Article

Bond Behavior and Failure Mechanisms of the Interface between Engineered Cementitious Composites and Shaped Steel

Jiaojiao Pan [1,2,*] , Zhenbin Huang [1,2], Tingting Lu [1,2] and Mingke Deng [3]

1   School of Civil Engineering, Xijing University, Xi'an 710123, China
2   Shaanxi Key Laboratory of Safety and Durability of Concrete Structures, Xi'an 710123, China; 2308590103019@stu.xijing.edu.cn (Z.H.); 20180173@xijing.edu.cn (T.L.)
3   School of Civil Engineering, Xi'an University of Architecture and Technology, Xi'an 710055, China; dengmingke@126.com
*   Correspondence: panjiaojiao01@126.com

Abstract: Due to their excellent ductility and crack-control ability, engineered cementitious composites (ECCs) combined with shaped steel can produce steel-reinforced engineering cementitious composite (SRECC) structures which exhibit significant advantages in prefabricated buildings. The interface bond behavior is the base for the cooperative working performance of the shaped steel and ECC. This study included push-out tests of one ordinary concrete control specimen and ten ECC specimens. The various parameters were the ECC compressive strength, fiber volume content, cover thickness, and the embedded length of shaped steel. The bond stress–slip curves at the loading and free end were obtained, and the effects of various parameters on the characteristic points of curves were analyzed. The results indicated that the ordinary concrete specimen failed in brittle splitting, with the cracks completely penetrating the surface of the specimen. Due to the fiber-bridging effect in ECCs effectively preventing the development and extension of cracks, the shaped steel at the free end was obviously pushed out, and the surrounding matrix maintained good integrity after testing finished. For ECC specimens, bond or splitting-bond failure occurred, exhibiting outstanding ductility. Compared with the ordinary concrete specimen, the standard ultimate and residual bond strength of ECC specimens improved by 37.9% and 27.4%, respectively. Besides the increase in ECC compressive strength, the fiber volume content and cover thickness had a significant positive influence on the ultimate and residual bond strength, whereas the effect of the embedded length was the opposite. Finally, the calculation equations of characteristic bond strength were proposed, and the calculated values matched well with the experimental values.

Keywords: bond strength; engineered cementitious composites; failure mechanism; shaped steel; push-out test

1. Introduction

Steel-reinforced concrete (SRC) structure [1,2] is a typical composite structure that exhibits high stiffness, excellent bearing capacity, and earthquake resistance and can reduce section sizes. Due to the advantages mentioned above, SRC structures have been widely used in buildings with a large span or heavy load or buildings in high-intensity fortification areas [3,4]. However, this structure type also has some problems in practical construction. Traditional SRC structures are composed of shaped steel and the surrounding reinforced concrete, which usually causes position conflicts between the shaped steel and reinforcing cage, especially in beam–column connections. Some methods have been adopted to avoid cutting the steel bars and stirrups, such as opening the holes in the flange and web of the shaped steel [5]. In this situation, the performance of shaped steel would be weakened in terms of flexural and shear resistance. Wu [6,7] tried to use the discrete steel fibers to substitute the reinforcing cages and proposed a new pattern of composite structure–steel

and steel fiber-reinforced concrete (SSFRC). Steel fiber-reinforced concrete (SFRC) [8,9] materials were prepared by adding steel fibers to the concrete. Steel fibers were able to improve the brittleness of concrete materials by delaying the appearance and extension of cracks. After removing the reinforcing cages, the cross-section of SSFRC specimens was effectively simplified and consequently ensured the pouring quality of concrete in the beam–column joints [10].

Engineered cementitious composites are superior to steel fiber-reinforced concrete in terms of ductility and damage-resistance capacity [11–13]. This material mainly consists of cement, fly ash, sand, fibers, and water, which shows obvious pseudo-strain hardening and multiple cracking behaviors under tensile and shear loads [14,15]. The application of ECC in composite structures could change the failure mode and improve the energy-dissipation and damage-tolerance ability [16–19]. In order to gain a deep knowledge of the co-working performance of the shaped steel and ECC, it is very necessary to investigate the bond behavior between these two materials. Numerous researchers have mainly focused on the bond properties of steel bars and ECC as a result of the earlier engineering applications of ECC in the strengthening and repairing of existing reinforced concrete buildings [20–23]. Pan [24] investigated the bond behavior of plain round bars embedded in ECC and concluded that only a small free-end slip occurred for specimens with plain round bars when the maximum bond stress was reached. Based on the pull-out tests, Feldman [25] concluded that the bond resistance of plain round bars mainly depended on the chemical adhesion and friction action but lacked the mechanical interlock in comparison with the ribbed bars. Chao [26] found that bond behavior was obviously improved for ECC specimens owing to the fiber-bridging effect effectively preventing the opening and extension of cracks. On the basis of the improved bond behavior, the cover thickness and the spacing of main steel bars [27], as well as the anchorage length of steel bars [28,29] in ECC components, could be reduced.

Scholars have begun a preliminary exploration of the interface bond properties between shaped steel and ECC. Bai [30] investigated the bond behavior between H-shaped steel and ECC and obtained the bond stress–slip curves at the loading end. The various parameters included the volume fraction of polyvinyl alcohol (PVA) fiber, stirrup reinforcement ratio, ECC cover thickness, and H-shaped steel embedded length. The results indicated that the ultimate bond stress was significantly affected by the PVA volume fraction and cover thickness, whereas the stirrup-reinforced ratio had little influence on the critical bond stress. Tian [31] tested the nine full-scale, H-shaped steel–ECC specimens and simulated the shaped steel–ECC interface by using cohesive finite elements. The experimental results showed that a splitting failure finally occurred for the ECC specimens with multiple splitting and intumescent cracks, and the outer flange of the H-shaped steel carried most of the push-out load.

Existing studies have concentrated on the bond behavior between shaped steel and ECC with reinforcing cages and tested the bond stress–slip curves at the loading end. This traditional composite structure type still faces the problem of construction difficulties due to the presence of reinforcing cages. Based on the design method of [5,6], this research tried to combine ECC with the shaped steel to produce SRECC structures without reinforcing cages by making use of its excellent ductility and crack-control ability. These new SRECC structures can reduce construction complexity and ensure structural quality, which exhibits significant advantages in prefabricated buildings. However, few investigations have been conducted on the bond mechanism and the failure mode between shaped steel and engineered cementitious composites without reinforcing cages. This is not beneficial to the practical engineering application of SRECC structures.

Eleven push-out tests were carried out in this study to evaluate the interface bond behavior and failure mechanism between the shaped steel and ECC without reinforcing cages. The design parameters were the ECC compressive strength, fiber volume content, cover thickness, and the embedded length of the shaped steel. The bond stress–slip curves at the loading and free end were obtained. Finally, based on the analysis of the influence of

various parameters on the bond properties, calculation equations for the initial, ultimate, and residual bond strengths were proposed.

2. Experimental Program

2.1. Materials

The constituents of ECC materials mainly consisted of ordinary Portland cement 42.5R, Class F fly ash, mineral powder, silica fume, silica sand, polyethylene (PE) fiber, and water. To evaluate the impact of ECC compressive strength and fiber volume content on the interface property, four different ECC mixtures were prepared for this study. Table 1 lists the performance indicators of PE fiber. The PE fiber is presented in Figure 1.

Table 1. Performance indicators of PE fiber.

Fiber Type	Length /mm	Diameter /μm	Tensile Strength /MPa	Elastic Modulus /GPa	Density /g·cm^{-3}
PE	12	43	1900	39	1.3

Figure 1. PE fiber.

Table 2 lists the mixture proportions of ECC by weight and the corresponding mechanical properties. Four ECC mixtures were marked as E1–1.5, E2–1.5, E1–0.5, and E1–1.0, respectively. According to previous research [32], 60 days of age was adopted to determine the performance indicators of ECC materials. The symbols f_{cu}, f_t, and ε_{tu} represented the compressive strength, tensile strength, and ultimate tensile strain of ECC at the age of 60 days, respectively. Referring to Table 2, it can be seen that mixtures E1–1.5 and E2–1.5 have great differences in terms of compressive strength. By changing the fiber volume content, the magnitude of the internal fiber-bridging stress of mixtures E1–1.5, E1–1.0, and E1–0.5 were distinct, and thus their ultimate tensile strain varied. Moreover, one concrete mixture, N1, was designed as the contrast. The mixture proportion of concrete by weight was cement: sand: coarse aggregate: water = 1.00:1.75:2.70:0.4, and the tested compressive strength was 63.9 MPa.

Table 2. Mixture proportions of ECC by weight and the corresponding mechanical properties.

Mixture	Binder				Water Binder Ratio	Sand Binder Ratio	PE Fibers	f_{cu} (MPa)	f_t (MPa)	ε_{tu}
	Cement	Fly Ash	Mineral Powder	Silica Fume						
E1–1.5	50%	50%	-	-	0.29	0.36	1.5%	55.4	5.1	3.2%
E2–1.5	55%	20%	20%	5%	0.24	0.36	1.5%	73.2	6.9	2.8%
E1–0.5	50%	50%	-	-	0.29	0.36	0.5%	56.3	5.2	0.6%
E1–1.0	50%	50%	-	-	0.29	0.36	1.0%	55.9	5.1	1.8%

Shaped steels with a section of HW 100 mm × 100 mm × 6 mm × 8 mm were adopted. Table 3 shows the mechanical properties of the shaped steel.

Table 3. Mechanical properties of the shaped steel.

| Steel	Location	Yield Strength /MPa	Ultimate Strength /MPa	Specific Elongation /%
Shaped steel	Web	275.56	409.26	36
	Flange	298.87	437.59	34

2.2. Specimen Design

In order to investigate the bond behavior of the interface between the shaped steel and ECC, eleven push-out specimens were fabricated. Table 4 shows the design parameters of all specimens. As contrast, one ordinary concrete specimen denoted as CC1 was prepared to clarify the difference between the ECC and concrete specimens. As seen in Table 4, various parameters are ECC compressive strength (E1, E2), fiber volume content (0.5%, 1.0%, 1.5%), cover thickness (30 mm, 40 mm, 50 mm, 60 mm), and the embedded length (300 mm, 400 mm, 500 mm, 600 mm) of the shaped steel. Figure 2 demonstrates the design details of specimens. The extension lengths of the shaped steel at both ends of the specimens were 50 mm. All specimens were cast horizontally and then were cured under natural conditions for 60 days until testing.

Table 4. Design parameters of specimens.

Specimen	Mixture	V_f (%)	C_{ss} (mm)	l_a (mm)	b (mm)
S1	E1–1.5	1.5	50	400	200
S2	E2–1.5	1.5	50	400	200
F1	E1–0.5	0.5	50	400	200
F2	E1–1.0	1.0	50	400	200
C1	E1–1.5	1.5	30	400	160
C2	E1–1.5	1.5	40	400	180
C3	E1–1.5	1.5	60	400	220
L1	E1–1.5	1.5	50	300	200
L2	E1–1.5	1.5	50	500	200
L3	E1–1.5	1.5	50	600	200
CC1	N1	–	50	400	200

Note: V_f is the fiber volume content; C_{ss} is the cover thickness; l_a is the embedded length of the shaped steel; b is the side size of cross-section.


(**a**) Cross-section   (**b**) Side view
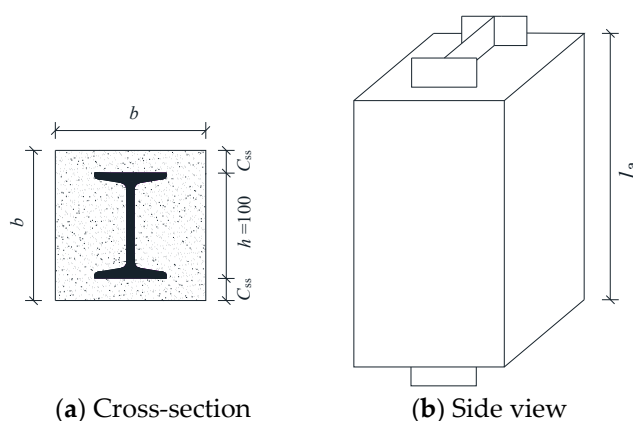
Figure 2. Design details of specimens (unit: mm).

2.3. Test Setup and Measurement

Figure 3 demonstrates the test setup in which the vertical load is applied by the MTS 200 t testing machine. By placing a special steel plate base under the bottom of the specimens and digging an H-type hole in the middle of the special base, it can be ensured that the shaped steel was pushed out from the surrounding matrix. The upper part of the

specimen that comes into direct contact with the testing machine is called the loading end, while the lower part is referred to as the free end. During the loading process, the shaped steel at the loading end is under pressure, while the matrix at the free end is compressive, thus achieving the push-out of the shaped steel from the surrounding matrix.
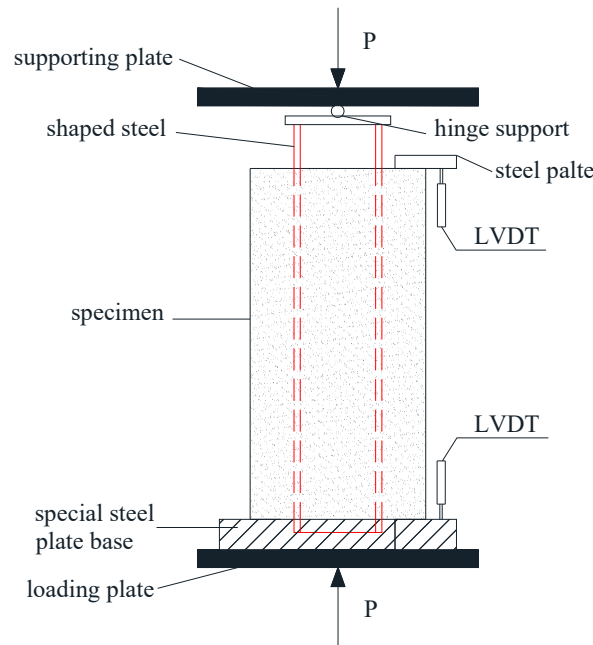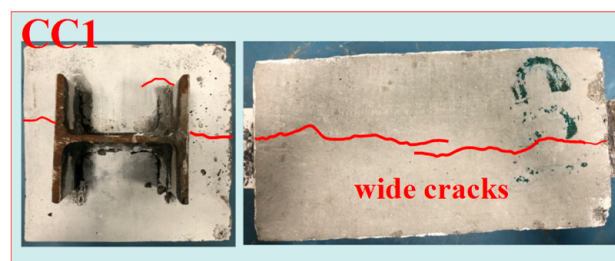

Figure 3. Test setup.

To measure the relative slip between the shaped steel and the surrounding matrix, two linear variable differential transformers (LVDTs) were installed at the loading and free end of the specimen, respectively. The displacement control with a rate of 0.5 mm/min was adopted. When the applied load declined and tended to stabilize, the test finished.

3. Experimental Results and Discussion

3.1. Failure Phenomena

(1)   Crack types

The final typical failure modes of all specimens are shown in Figure 4. On the basis of the loading process and the final failure modes, it can be found that the cracks in all specimens can be grouped into two types (i.e., a splitting crack and a bond crack). The number of the crack and the final damage patterns of the specimens are shown in Table 5.
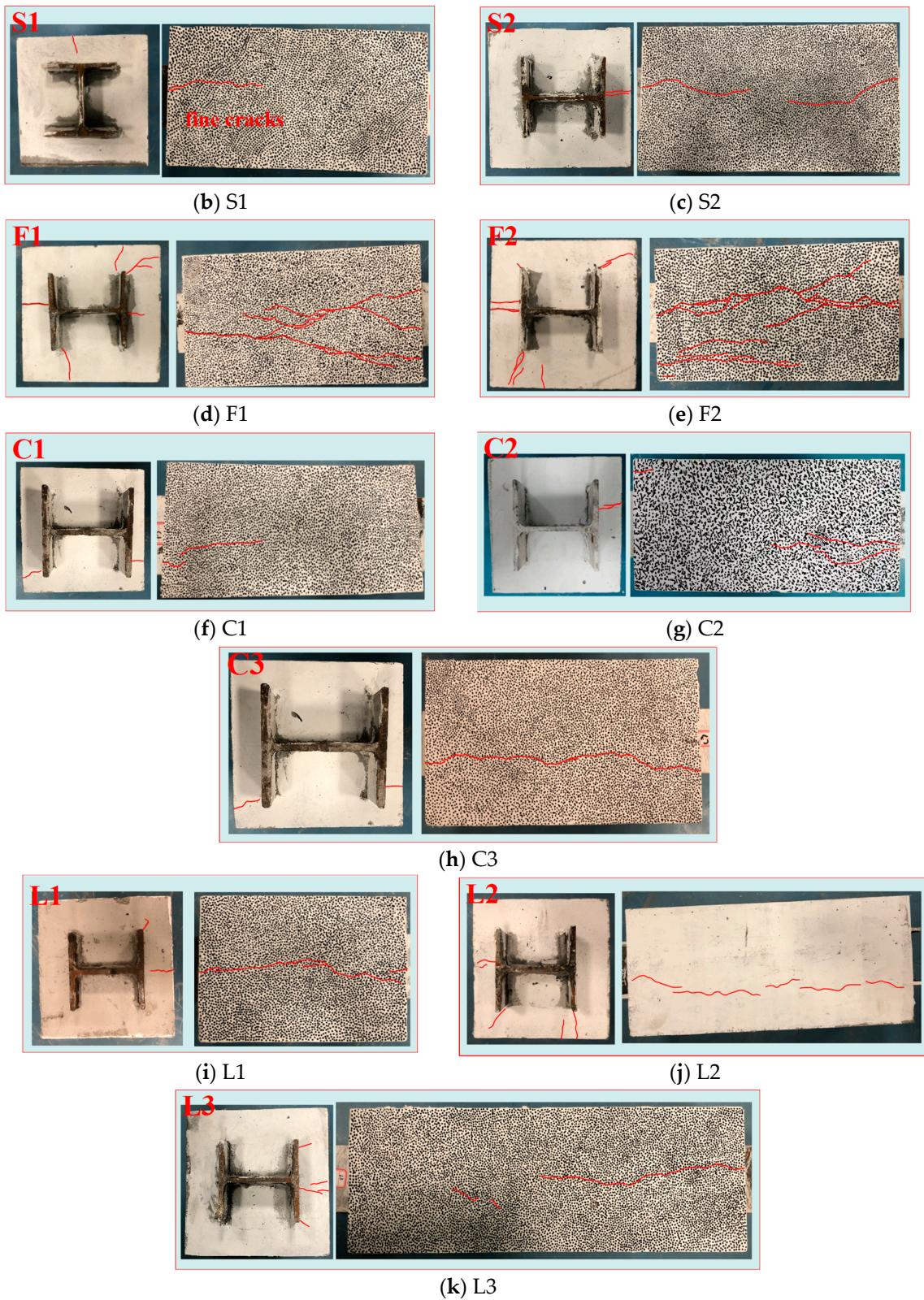

(a) CC1

Figure 4. *Cont.*

(**b**) S1

(**c**) S2

(**d**) F1

(**e**) F2

(**f**) C1

(**g**) C2

(**h**) C3

(**i**) L1

(**j**) L2

(**k**) L3

Figure 4. Typical failure modes.

Table 5. Experimental results.

Specimen	P_s/kN	P_u/kN	P_r/kN	τ_s/MPa	τ_u/MPa	τ_r/MPa	Number of Cracks		Failure Mode	Calculated Value/MPa		
							Tip of Flange	Middle of Flange		τ_s	τ_u	τ_r
S1	92.12	300.45	202.77	0.39	1.29	0.87	0	1	Bond	0.35	1.13	0.76
S2	107.66	331.59	228.28	0.46	1.42	0.98	0	2	Bond	0.43	1.40	0.94
F1	68.51	215.24	135.62	0.29	0.92	0.58	3	2	Splitting-bond	0.33	0.97	0.64
F2	77.98	274.22	191.62	0.33	1.17	0.82	4	2	Splitting-bond	0.34	1.05	0.70
C1	57.98	182.55	125.62	0.25	0.78	0.54	1	1	Bond	0.24	0.82	0.57
C2	77.15	266.02	165.57	0.33	1.14	0.71	0	1	Bond	0.29	0.98	0.67
C3	85.64	293.69	186.62	0.37	1.26	0.80	1	1	Splitting-bond	0.35	1.13	0.76
L1	60.27	188.79	127.04	0.34	1.08	0.73	1	1	Splitting-bond	0.35	1.14	0.77
L2	103.81	336.35	217.69	0.36	1.15	0.75	3	1	Bond	0.35	1.13	0.75
L3	130.23	406.77	263.03	0.37	1.16	0.75	2	2	Bond	0.35	1.13	0.75
CC1	72.65	234.69	171.34	0.31	1.00	0.73	0	2	Splitting	/	/	/

Note: P_s is initial load when the shaped steel at the free end begins to slip; P_u is the ultimate load at the peak point of the bond stress–slip curves; P_r is the residual load when the bond stress–slip curve tends to stabilize; τ_s, τ_u, and τ_r are the corresponding initial bond strength, ultimate bond strength, and residual bond strength, respectively.

During the push-out process, the shaped steel will exert an extrusion force on the surrounding ECC. Under the action of the radial force of this extrusion pressure, the expansion tensile stress is generated in ECC. When the expansion tensile stress exceeded the tensile strength of ECC, a splitting crack formed. This type of crack first appeared on the outer surface of the specimen where the cover thickness was the smallest (that is, in the middle of the flange) and then developed from the outside inwards in a direction perpendicular to the flange. The splitting crack gradually changed from wide to narrow along the outer surface of the specimens toward the flange.

In addition, the bond crack formed at the tips of the flange because of the extrusion of the shaped steel against the ECC. The bond crack extended to the outer surface of the specimens at 45° or parallel to the flange of the shaped steel. The bond crack gradually narrowed along the tips of the flange toward the surface of the specimens.

(2)　Failure mode

For ordinary concrete specimens, there was no crack in the initial loading process. With the increase in the push-out load, the splitting cracks began to appear in the middle of the flange at the loading end and gradually extended to the free end. Then, with a "bang", the width and length of the crack increased rapidly. The ordinary concrete specimen underwent a typical brittle splitting failure (see Figure 4a). Figure 5 demonstrates the interface at the free end between the shaped steel and matrix for the ordinary concrete and ECC specimens after the test. In Figure 5a, it can be seen that the concrete at the tip of the flange is crushed. The shaped steel and concrete at the web were obviously detached, resulting in a large gap at the interface.

For ECC specimens, cracks appeared in the middle or tips of the flange. As shown in Figure 4, only one splitting crack appeared at the loading end for specimens S1, S2, and C2. The longitudinal cracks on the surface of specimens are very fine and short in length, and finally, the bond failure occurs. For specimens C1, L2, and L3, both the bond crack and the splitting crack appeared at the loading end. The splitting crack on the surface of the specimens did not penetrate, and the failure modes of these specimens were still bond failures. However, the same phenomenons were observed in specimens F1, F2, C3, and L1; the splitting crack on the surface of these specimens fully penetrated, and splitting-bond failure occurred.

As can be seen in Figure 5b, the shaped steel at the free end is obviously pushed out, and the surrounding matrix still maintains good integrity after the test is finished. This phenomenon indicated that the fiber-bridging effect effectively prevented the development and extension of cracks, and the failure form of ECC specimens exhibited excellent ductility. It is worth noting that the cracks in specimens F1 (V_f = 0.5%) and F2 (V_f = 1.0%) were numerous and fine. This was due to the fact that the fiber volume contents in these two specimens were relatively small, and the constrainment of fiber-bridging stress on the

crack was also weak. Therefore, the cracks were sufficiently developed, and the main crack width was larger.

(**a**) Ordinary concrete specimen

(**b**) ECC specimen
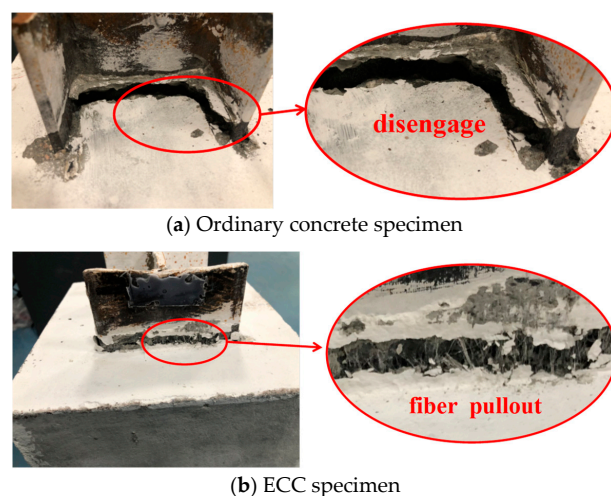
Figure 5. Interface between the shaped steel and matrix at the free end.

3.2. Bond Stress–Slip Curves

The experiments tested the relative slip at the interface between the shaped steel and the matrix, both at the loading and free end. With the increase in the applied load, the slip at the loading end and free end did not increase synchronously. The slip of the loading end occurred relatively early and was always ahead of that of the free end. This suggested that the bond stress was not uniformly distributed along the embedded length of the shaped steel. The same conclusion was obtained in other research [7].

Considering the simplicity of calculation and analysis, the average bond stress [30] over the embedded length of the shaped steel is widely adopted by Equation (1). Its calculation formula is

$$\tau = \frac{P}{Cl_a} \tag{1}$$

where τ is the average bond stress; P is the push-out load; C is the cross-section perimeter of the shaped steel; l_a is the embedded length of the shaped steel.

Figure 6 displays the bond stress–slip curves of all specimens. An existing study [28] demonstrated that the surface roughness of the shaped steel was comparable to that of the plain round bar. The chemical adhesion and sliding friction mainly contribute to the interface bond between the shaped steel and the matrix. As shown in Figure 5, the bond stress–slip curves consist of five distinct parts: a non-slip stage, linear ascent stage, nonlinear ascent stage, descent stage, and residual stage.

(1)　Non-slip stage

At the initial stage, the bond resistance between the shaped steel and the surrounding matrix was primarily provided by the chemical adhesive force. No slip occurred at both ends of the specimen.

(2)　Linear ascent stage

As the push-out load increased, the interface chemical adhesive force began to be destroyed. The slip first appeared at the loading end. With further loading, the interface failure gradually extended to the free end. Until the chemical adhesive between the shaped steel and the matrix was completely destroyed, the shaped steel at the free end began to slip. At this time, the push-out load was about 30% of the ultimate load.

(3)　Nonlinear ascent stage

As the load further increased, the bond resistance at the interface was mainly provided by the sliding friction between the shaped steel and the matrix. The bond stress–slip curve

entered the nonlinear ascent stage, and the cracks began to appear in the specimen. With the increase in the pull-out load, the cracks developed rapidly. The gripping force of the surrounding matrix on the shaped steel gradually weakened, which led to a steady reduction in the slope of the curve. When the sliding friction of the interface reached the maximum, the curve reached the peak point.

(4) Descent stage

During this stage, the shaped steel was progressively pushed out. The slip at the loading end and free end increased steadily, which led to a reduction in the roughness of the interface and a constant drop in the friction coefficient at the interface. As a result, the bond stress–slip curve began to decline.

(5) Residual stage

When the load dropped to 60~80% P_u, the contact surface between the shaped steel and the matrix became progressively smoother. The slip at the loading and free end was virtually synchronized. In this stage, the slip consistently increased while the load fell slowly. The bond stress–slip curve gradually flattened out.
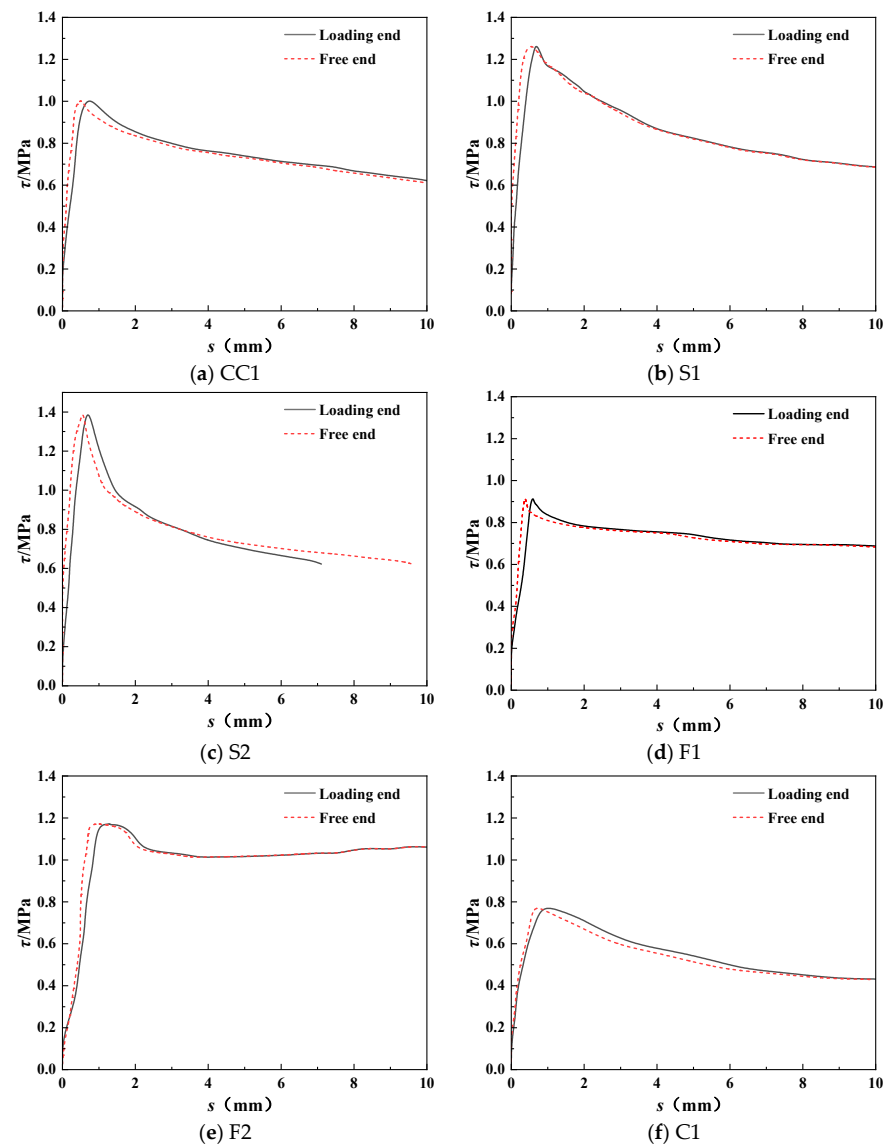

Figure 6. *Cont.*

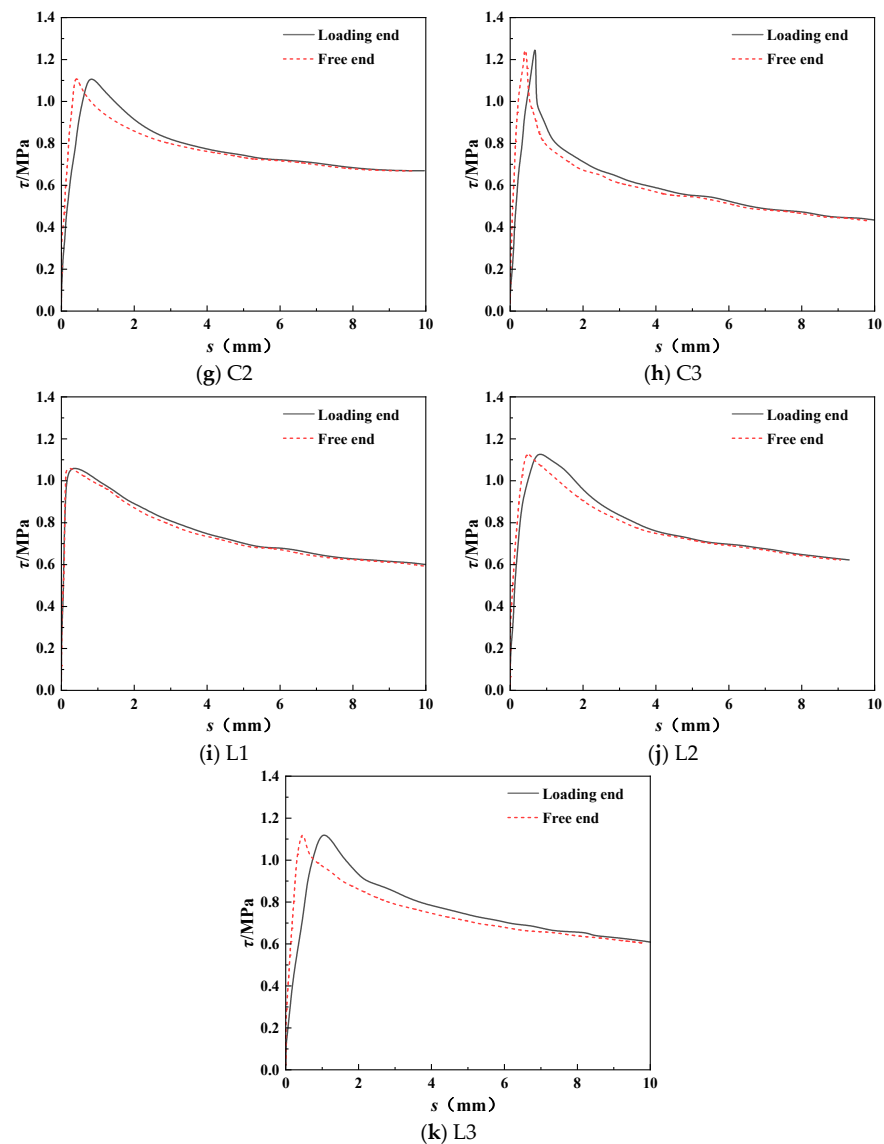**Figure 6.** Bond stress–slip curves.

4. Analysis of the Characteristic Points of the Bond Stress–Slip Curves

4.1. Comparison between ECC and the Ordinary Concrete

In Table 2, it can be seen that the compressive strengths of specimens S1 and CC1 are 55.4 and 63.9 MPa, respectively. In order to eliminate the impact of matrix compressive strength, Equation (2) was commonly used to calculate the standard bond stress [30].

$$\overline{\tau} = \frac{\tau}{\sqrt{f\text{cu}}} \tag{2}$$

where $\overline{\tau}$ is the standard bond stress.

Table 5 summarizes the characteristic points of the bond stress–slip curve for all specimens. Based on the calculation of Equation (2), the standard ultimate bond strengths of specimens S1 and CC1 were 0.17 and 0.13 MPa, respectively, and the standard residual bond strengths were 0.12 and 0.09 MPa, respectively.

Under the condition of the same embedded length and cover thickness, the standard ultimate bond strength of specimen S1 was enhanced by 37.9% compared to the ordinary concrete specimen CC1. This was mainly related to the binder components of ECC materials. For ordinary concrete, the cement during the hydration process would generate a large

amount of Ca(OH)$_2$. Ca(OH)$_2$ exhibited slight solubility in water, and upon reaching saturation in solution, it precipitated as a hexagonal plate or layered crystal, resulting in a relatively rough surface structure on the shaped steel. As a result, the chemical adhesion at the interface between the shaped steel and the concrete was poor. Fifty percent fly ash is incorporated into the ECC, as shown in Table 2. The main mineral component (SiO$_2$) can react with the hydration product of cement (Ca(OH)$_2$) to produce C-S-H gel with strong gelling, thereby enhancing the chemical adhesion and sliding friction of the interface between ECC and the shaped steel.

The standard residual bond strength of specimen S1 was enhanced by 27.4% compared to the ordinary concrete specimen CC1. This phenomenon can be explained by the following reasons. The bond resistance was mainly provided by the sliding friction during the residual stage. Due to the outstanding crack control ability and damage resistance ability, ECC still maintained good integrity during the residual stage, and its gripping effect on the shaped steel was obviously better than that of ordinary concrete. Therefore, the sliding friction force of the ECC specimen was higher than that of the ordinary concrete specimen.

4.2. Effects of Various Parameters

Figure 7 demonstrates the effects of various parameters on the characteristic points of the bond stress—slip curves.
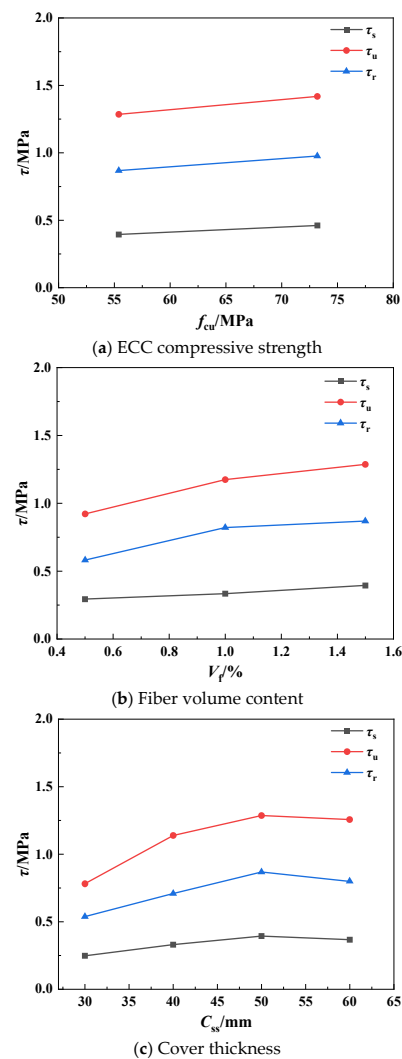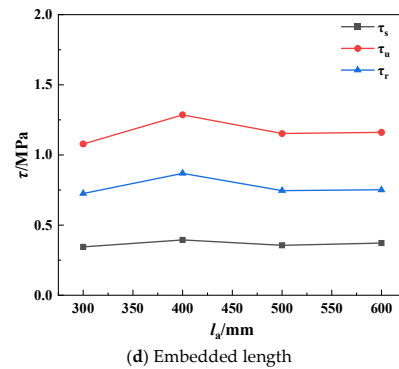

(**a**) ECC compressive strength

(**b**) Fiber volume content

(**c**) Cover thickness

Figure 7. *Cont.*

(**d**) Embedded length

Figure 7. Effects of various parameters on the characteristic points of the bond stress–slip curves.

(1)   ECC compressive strength

As the ECC compressive strength increased, the initial, ultimate, and residual bond strength exhibited an improvement trend (see Figure 7a). Compared with specimen S1, the initial, ultimate, and residual bond strength of specimen S2 enhanced by 16.87%, 10.36%, and 12.58%, respectively. This suggested that the increase in the ECC compressive strength played an important role in improving the bond property of the interface between the shaped steel and ECC.

(2)   Fiber volume content

The fiber volume content for the specimens F1, F2, and S1 was 0.5%, 1.0%, and 1.5%, respectively. Compared with F1, the initial bond strength of F2 and S1 was increased by 13.82% and 34.46%, respectively. The ultimate bond strength increased by 27.40% when the fiber volume content increased from 0.5% to 1.0% and only increased by 9.57% when the fiber volume content increased from 1.0% to 1.5%. This phenomenon indicated that the improvement effect of increasing the fiber volume content on the ultimate bond strength was limited when the fiber volume content exceeded 1.0%.

With the increase in the fiber volume content from 0.5% to 1.0%, the residual bond strength of the specimen increased by 41.29%. This was due to the increase in the fiber volume content, resulting in a significant enhancement in the fiber-bridging stress within the matrix, effectively restricting the propagation of splitting cracks and bond cracks during the push-out process of the shaped steel. This ultimately improved the bond property of the interface. The residual bond strength of the specimens showed only a marginal 5.82% increase with the addition of fiber volume content from 1.0% to 1.5%. These findings suggest that the enhancement in the fiber volume content had minimal impact on the residual bond strength when the fiber volume content exceeded 1.0%.

(3)   Cover thickness

As shown in Figure 7c, when the cover thickness is less than 50 mm, the initial, ultimate, and residual bond strength continue to increase with the increase in the cover thickness. This can be attributed to the fact that the greater the thickness of the cover thickness, the more obvious the constraint effect on cracks. Once the cover thickness exceeded 50 mm, the constraint effect reached the maximum. As a result, the ultimate and residual bond strength no longer increased. Thus, the critical relative cover thickness (C_{ss}/h) was selected as 0.5.

(4)   Embedded length

The maximum initial, ultimate, and residual bond strength are observed when the embedded length of the shaped steel is 400 mm, as depicted in Figure 7d. When the embedded length of the shaped steel exceeded 400 mm, there was a gradual decrease in both ultimate and residual bond strength, which tended to stabilize with a further increase in embedded length.

Based on the analysis in Section 2.2, it was determined that the bond stress was unevenly distributed along the embedded direction of the shaped steel. What was calculated in this study was the average bond stress over the whole embedded length (see Equation (1)). When the embedded length of the shaped steel was less than 400 mm, the proportion of the high bond stress area along the embedded direction of the shaped steel was larger, resulting in an increasing trend in the bond strength as the embedded length ranged from 300 mm to 400 mm. However, beyond 400 mm, the proportion of the high bond stress area reduced progressively, concurrent with a continuous expansion of the low bond stress area, leading to a decline in bond strength with a further increase in the embedded length. When the embedded length exceeded 500 mm, the bond strength tended to stabilize. Consequently, the critical relative embedded length (l_a/h) of the shaped steel in ECC was determined to be 5.

5. Calculation Method of Bond Strength

Based on the analysis of the experimental results, it can be found that the bond strength was closely correlated with the ECC compressive strength, fiber volume content, cover thickness, and the embedded length of the shaped steel. Through the regression analysis using the least square method on experimental data, calculation equations for the initial, ultimate, and residual bond strength were proposed.

$$\tau_s = (0.0021 + 0.0275 C_{ss}/h - 0.0001 l_a/h + 0.0011 V_f) f_{cu}{}^{0.75} \tag{3}$$

$$\tau_u = (0.0051 + 0.0768 C_{ss}/h - 0.0002 l_a/h + 0.0081 V_f) f_{cu}{}^{0.75} \tag{4}$$

$$\tau_r = (0.0071 + 0.0455 C_{ss}/h - 0.0004 l_a/h + 0.0057 V_f) f_{cu}{}^{0.75} \tag{5}$$

when $C_{ss}/h \geq 0.5$, C_{ss}/h is taken as equal to 0.5; when $l_a/h \geq 5$, l_a/h is taken as equal to 5.

The calculated values of the characteristic bond strength are presented in Table 5. The correlation coefficient between the calculated and experimental value in terms of the initial, ultimate, and residual bond strength were 0.898, 0.880 and 0.895, respectively. Figure 8 demonstrates the comparison between the calculated and experimental values. In Figure 8, it can be seen that the calculated results agree well with the experimental results. This phenomenon indicates that the proposed calculated equations in this research could effectively predict the characteristic bond strengths between the shaped steel and ECC.
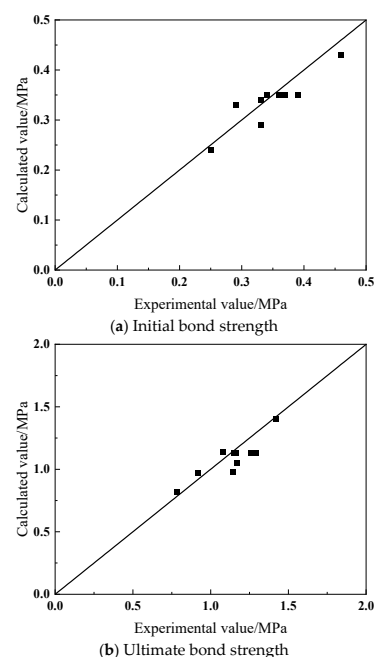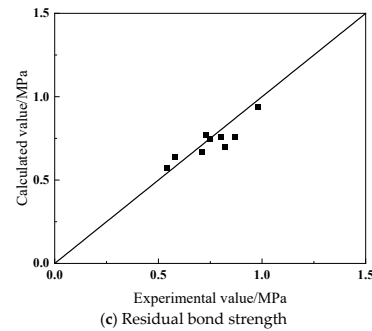

(a) Initial bond strength

(b) Ultimate bond strength

Figure 8. *Cont.*

(c) Residual bond strength

Figure 8. Comparison between calculated value and experimental value.

6. Conclusions

This study fabricated eleven push-out specimens to evaluate the bond behavior between the shaped steel and ECC. The design parameters were the ECC compressive strength, fiber volume content, cover thickness, and the embedded length of the shaped steel. The following conclusions were drawn from the experimental results.

(1) The ordinary concrete specimen failed in brittle splitting. However, the fiber-bridging effect effectively controlled crack development and extension, allowing the surrounding matrix to maintain good integrity after testing. In contrast, ECC specimens exhibited splitting-bond or bond failure, demonstrating excellent ductility.

(2) The bond stress–slip curves consisted of five stages: non-slip, linear ascent, nonlinear ascent, descent, and residual stages. During the initial loading stage, the bond resistance was primarily provided by the chemical adhesive force, with no slip occurring at both ends of the specimen. As the load further increased, the interface chemical adhesive force was destroyed and the bond resistance was mainly provided by sliding friction.

(3) Compared to the ordinary concrete specimen, the standard ultimate and residual bond strength of the ECC specimen were enhanced by 37.9% and 27.4%, respectively, due to the reactivity of fly ash's main mineral component SiO_2 with the cement hydration product $Ca(OH)_2$, resulting in the formation of strong gelling C-S-H gel. Consequently, the chemical adhesive and sliding friction at the interface between ECC and the shaped steel were enhanced.

(4) The increase in the ECC compressive strength, fiber volume content, and cover thickness had a positive influence on the initial, ultimate, and residual bond strength of ECC specimens. The maximum initial, ultimate, and residual bond strength was achieved when the embedded length of the shaped steel was 400 mm.

(5) The calculation equations for characteristic bond strengths were built through the regression analysis of experimental data. The comparison between the calculated and experimental values suggested that the proposed equations were capable of effectively predicting the characteristic bond strengths between the shaped steel and ECC.

Author Contributions: Conceptualization, formal analysis, writing—review and editing, J.P.; funding acquisition, J.P.; data curation, Z.H.; formal analysis and supervision, T.L. and M.D. All authors have read and agreed to the published version of the manuscript.

Data Availability Statement: The data that support this study are available from the corresponding author upon reasonable request.

References

1. Gan, D.; Guo, L.; Liu, J.; Zhou, X. Seismic behavior and movement strength of tubed steel reinforced-concrete (SRC) beams-columns. *J. Constr. Steel Res.* **2011**, *67*, 1516–1524. [CrossRef]
2. Hsu, H.L.; Hsieh, J.C.; Juang, J.L. Seismic performance of steel-encased composite members with strengthening cross-inclined bars. *J. Constr. Steel Res.* **2004**, *60*, 1663–1679. [CrossRef]
3. Shi, X.M.; Xie, N.; Fortune, K.; Gong, J. Durability of steel reinforced concrete in chloride environments: An overview. *Constr. Build. Mater.* **2012**, *30*, 125–138. [CrossRef]
4. Boyd, P.F.; Cofer, W.F.; Mclean, D.I. Seismic performance of steel-encased concrete columns under flexural loading. *ACI Struct. J.* **1995**, *92*, 355–364.
5. Yang, Y.; Yu, Y.L.; Guo, Y.X. Experimental study on shear performance of partially precast Castellated Steel Reinforced Concrete (CPSRC) beams. *Steel Compos. Struct.* **2016**, *21*, 289–302. [CrossRef]
6. Wu, K.; Chen, F.; Lin, J.; Zhao, J.; Zheng, H. Experimental study on the interfacial bond strength and energy dissipation capacity of steel and steel fibre reinforced concrete (SSFRC) structures. *Eng. Struct.* **2021**, *235*, 112094. [CrossRef]
7. Wu, K.; Zheng, H.; Shi, N.; Chen, F.; Xu, J. Analysis of the bond behavior difference in steel and steel fiber reinforced concrete (SSFRC) composite member with circular section. *Constr. Build. Mater.* **2020**, *264*, 120142. [CrossRef]
8. Prakash, A.; Srinivasan, S.M.; Rama, M.R.A. Application of steel fibre reinforced cementitious composites in high velocity impact resistance. *Mater. Struct.* **2017**, *50*, 6. [CrossRef]
9. Paultre, P.; Eid, R.; Langlois, Y.; Levesque, Y. Behavior of steel fiber-reinforced highstrength concrete columns under uniaxial compression. *J. Struct. Eng.* **2010**, *136*, 1225–1235. [CrossRef]
10. Wu, K.; Chen, F.; Chen, C.; Zheng, H.; Xu, J. Analysis of the Bearing and Damage Mechanism in Steel-Steel Fiber-Reinforced Concrete-Composite Member. *J. Mater. Civ. Eng.* **2020**, *32*, 04020274. [CrossRef]
11. Li, V.C. From Micromechanics to Structural Engineering—The Design of Cementitious Composites for Civil Engineering Applications. *Proc. Jpn. Soc. Civ. Eng.* **1992**, *10*, 37–48.
12. Wang, S.; Li, V.C. High early strength engineered cementitious composites. *ACI Mater. J.* **2006**, *103*, 97–105.
13. Li, V.C. Interface Tailoring for Strain-hardening PVA-ECC. *ACI Mater. J.* **2011**, *99*, 463–472.
14. Li, L.Z.; Cai, Z.W.; Yu, K.Q.; Zhang, Y.X.; Yao, Q. Performance-based design of all-grade strain hardening cementitious composites with compressive strengths from 40 MPa to 120 MPa. *Cem. Concr. Comp.* **2019**, *97*, 202–217. [CrossRef]
15. Lu, C.; Yuan, Z.; Yang, C.; Hou, D.; Yao, Y. Tensile properties of PVA and PE fiber reinforced engineered cementitious composites containing coarse silica sand. *J. Build. Eng.* **2023**, *75*, 106913. [CrossRef]
16. Kabir, M.I.; Lee, C.K.; Rana, M.M.; Zhang, Y.X. Flexural and bond-slip behaviours of engineered cementitious composites encased steel composite beams. *J. Constr. Steel Res.* **2019**, *157*, 229–244. [CrossRef]
17. Fan, J.; Gou, S.; Ding, R.; Zhang, J.; Shi, Z. Experimental and analytical research on the flexural behaviour of steel-ECC composite beams under negative bending moments. *Eng. Struct.* **2020**, *210*, 110309. [CrossRef]
18. Yan, Y.; Liang, H.; Lu, Y.; Huang, Y. Behaviour of concrete-filled steel-tube columns strengthened with high-strength CFRP textile grid-reinforced high-ductility engineered cementitious composites. *Constr. Build. Mater.* **2021**, *269*, 121283. [CrossRef]
19. Rana, M.M.; Lee, C.K.; Al-Deen, S.; Zhang, Y.X. Flexural behaviour of steel composite beams encased by engineered cementitious composites. *J. Constr. Steel Res.* **2018**, *143*, 279–290. [CrossRef]
20. Hung, C.C.; Chen, Y.S. Innovative ECC jacketing for retrofitting shear-deficient RC members. *Constr. Build. Mater.* **2016**, *111*, 408–418. [CrossRef]
21. Deng, M.K.; Zhang, Y.X. Cyclic loading tests of RC columns strengthened with high ductile fiber reinforced concrete jacket. *Constr. Build. Mater.* **2017**, *153*, 986–995. [CrossRef]
22. Parra-Montesinos, G.J.P.; Peterfreund, S.W.; Chao, S.H. Highly damage-tolerant beam-column joints through use of high-performance fiber-reinforced cement composites. *ACI Struct. J.* **2005**, *102*, 487–495.
23. Fischer, G.; Li, V.C. Deformation Behavior of Fiber-Reinforced Polymer Reinforced Engineered Cementitious Composite (ECC) Flexural Members under Reversed Cyclic Loading Conditions. *ACI Struct. J.* **2003**, *100*, 25–35.
24. Pan, J.J.; Deng, M.K.; Sun, H.Z. Bond behavior of plain round bar embedded in high ductile concrete under monotonic and cyclic loading. *Struct. Concr.* **2021**, *22*, 3446–3460. [CrossRef]
25. Feldman, L.R.; Bartlett, F.M. Bond strength variability in pullout specimens with plain reinforcement. *ACI Struct. J.* **2005**, *102*, 860–867.
26. Chao, S.H.; Naaman, A.E.; Parra-Montesinos, G.J. Bond Behavior of Reinforcing Bars in Tensile Strain-Hardening Fiber-Reinforced Cement Composites. *ACI Struct. J.* **2009**, *106*, 897–906.

27. Toshiyuki, K.; Hiroshi, H. Bond-Splitting Strength of Reinforced Strain-Hardening Cement Composite Elements with Small Bar Spacing. *ACI Struct. J.* **2015**, *112*, 189–198.

28. Choi, W.C.; Jang, S.J.; Yun, H.D. Bond and cracking behavior of lap-spliced reinforcing bars embedded in hybrid fiber reinforced strain-hardening cementitious composite (SHCC). *Compos. Part B-Eng.* **2017**, *108*, 35–44. [CrossRef]

29. Lee, S.W.; Kang, S.B.; Tan, K.H.; Yang, E.H. Experimental and analytical investigation on bond-slip behaviour of deformed bars embedded in engineered cementitious composites. *Constr. Build. Mater.* **2016**, *127*, 494–503. [CrossRef]

30. Bai, L.; Yu, J.; Zhang, M.; Zhou, T. Experimental study on the bond behavior between H-shaped steel and engineered cementitious composites. *Constr. Build. Mater.* **2019**, *196*, 214–232. [CrossRef]

31. Tian, L.M.; Kou, Y.F.; Lin, H.L.; Li, T.J. Interfacial bond-slip behavior between H-shaped steel and engineered cementitious composites (ECCs). *Eng. Struct.* **2021**, *231*, 111731. [CrossRef]

32. Deng, M.K.; Pan, J.J.; Sun, H.Z. Bond behavior of steel bar embedded in Engineered Cementitious Composites under pullout load. *Constr. Build. Mater.* **2018**, *168*, 705–714. [CrossRef]